Engineering 30 (2023) 153–160

Contents lists available at ScienceDirect

Engineering

journal homepage: www.elsevier.com/locate/eng

Research
Textile Engineering—Article

Scalable Core–Sheath Yarn for Boosting Solar Interfacial Desalination through Engineering Controllable Water Supply

Xingfang Xiao [#], Luqi Pan [#], Tao Chen, Manyu Wang, Lipei Ren, Bei Chen, Yingao Wang, Qian Zhang [*], Weilin Xu [*]

State Key Laboratory of New Textile Materials and Advanced Processing Technologies, School of Textile Science and Engineering, National Local Joint Laboratory for Advanced Textile Processing and Clean Production, Wuhan Textile University, Wuhan 430200, China

ARTICLE INFO

Article history:
Received 6 November 2022
Revised 26 March 2023
Accepted 26 March 2023
Available online 7 June 2023

Keywords:
Interfacial solar desalination
Photothermal yarn
Tunable water supply
Core–sheath yarn
Salt clogging

ABSTRACT

Tailoring water supply to achieve confined heating has proven to be an effective strategy for boosting solar interfacial evaporation rates. However, because of salt clogging during desalination, a critical point of constriction occurs when controlling the water rate for confined heating. In this study, we demonstrate a facile and scalable weaving technique for fabricating core–sheath photothermal yarns that facilitate controlled water supply for stable and efficient interfacial solar desalination. The core–sheath yarn comprises modal fibers as the core and carbon fibers as the sheaths. Because of the core–sheath design, remarkable liquid pumping can be enabled in the carbon fiber bundle of the dispersed superhydrophilic modal fibers. Our woven fabrics absorb a high proportion (92%) of the electromagnetic radiation in the solar spectrum because of the weaving structure and the carbon fiber sheath. Under one-sun (1 $kW \cdot m^{-2}$) illumination, our woven fabric device can achieve the highest evaporation rate (of 2.12 $kg \cdot m^{-2} \cdot h^{-1}$ with energy conversion efficiency: 93.7%) by regulating the number of core–sheath yarns. Practical application tests demonstrate that our device can maintain high and stable desalination performance in a 5 wt% NaCl solution.

1. Introduction

Clean water is vital for mankind's survival [1–3]. However, as populations grow and industrialization intensifies, providing sufficient supplies of freshwater continues to be a significant challenge for society and governments. Different approaches [4–7] have been utilized to address the challenges of the global freshwater crisis. Among these is solar interface evaporation (SIE) technology [8,9], which localizes solar-thermal conversion and steam generation near the air-absorber interface; SIE offers high conversion efficiency and eco-friendly characteristics, and is a promising strategy for the purification of water. Over the past several years, intriguing photothermal materials and structures such as nanomaterials [10–14] and bionic structures [15–17] have been exploited for efficient photothermal conversion. These highly effective SIE technologies share the following merits [18–20]: ① greater than 90% absorptivity over the entire solar spectrum for an ideal photothermal conversion, ② optimized water channels for maintaining consistent supply of water for stable steam generation, and ③ a relatively low thermal conductivity for preventing heat loss to the water.

Excessive water transport, generally overlooked in conventional designs, causes heat loss in absorbers; this limits the evaporation rate [21–24]. To solve this problem, a key control point is water supply balancing in the photothermal evaporator. Two main working mechanisms are employed to control the water flow: passive [24–29] and active [21,28,30]. In a typical passive balanced water supply, hydrophobic materials are used in the water supply channels to optimize water transport speeds [25,26] and to improve photothermal conversion efficiency. In addition, water transport is confined to the outer surface area rather than to the large, inner, and interconnected pores of the porous photothermal evaporators. These photothermal evaporators can potentially offer control of water flow for a highly efficient interfacial evaporation process. In an active system, balanced water flow can be achieved by indirectly adjusting the external water flow rate [21,30]. However, dur-

* Corresponding authors.
E-mail addresses: qzhang@wtu.edu.cn (Q. Zhang), weilin_xu@wtu.edu.cn (W. Xu).
[#] These authors contributed equally to this work.

https://doi.org/10.1016/j.eng.2023.03.015

ing desalination, the stability and durability of these devices has not been considered in either the passive or active designs because balanced water flow limits the water content in the absorbers, causing salt accumulation. Therefore, an optimally balanced water flow for evaporators could simultaneously improve evaporation performance and achieve durable salt rejection during desalination in a facile and scalable manner to meet practical requirements.

In this study, we propose the novel concept of core–sheath yarn (CSY) for controllable water flow to improve evaporation during desalination. Fig. 1 illustrates the solar interfacial desalination process of the CSY-woven fabric (CSY-F). The CSY is designed with two layers: a carbon fiber-based photothermal fiber sheath that can serve as an absorber [31–33] for solar energy capture, and a core layer of super-hydrophilic modal yarn that can enhance the water supply of the carbon fiber sheath. The CSY (acting as a warp) and carbon fiber (acting as a weft) were used to fabricate a fabric-based evaporator, in which the CSY served as a water channel. Balanced water flow in this fabric-based evaporator can easily be achieved by adjusting the number of modal yarns in the CSYs during the weaving process. This is because of the poor water pumping caused by the dense surface and lower polar surface energy of the carbon fiber [34–36]. Balanced water flow can therefore enable stable and efficient solar interfacial desalination. Because the developed yarn and fabric were fabricated via traditional textile technology, a device based on the core-sheath yarn is practical and scalable.

2. Methods

2.1. Fabrication of CSY

First, water-soluble vinylon yarns (14.6 tex) were wound on the surface of carbon fiber yarns (60 tex) using a fancy spinning small sample machine to form a vinylon yarn/carbon fiber commingled yarn (VCCY). The parameters of the twister were as follows: ① hollow spindle speed = 3000 revolutions per minute (rpm); ② front roller speed = 10.07 $m{\cdot}min^{-1}$; ③ ring spindle speed = 1400 rpm; ④ middle front roller speed = 1.95 $m{\cdot}min^{-1}$; ⑤ delivery roller speed = 6.67 $m{\cdot}min^{-1}$; and ⑥ middle rear roller speed = 1.30 $m{\cdot}min^{-1}$. Second, a two-dimensional (2D) braiding machine was used to braid the VCCYs with the sheath and modal yarns (40 tex) as the core, forming CSYs.

2.2. Fabrication of fabric-based evaporator

The CSY-F was woven using an SGA598 semi-automatic weaving machine (manufactured by Jiangyin Tongyuan Textile Machinery Co. Ltd., China); weaving was carried out using the plain pattern. The CSYs prepared as warps were arranged in the warp direction to go through loom heddles and reeds; carbon fiber yarns (360 tex) were used as wefts to insert tensional warps. The warp and weft densities were 46 and 50 yarns per 10 cm, respectively. Subsequently, a piece of plain weave CSY-F was formed. The produced CSY-F was placed in water warmer than 20 °C and washed until the vinylon yarns on the carbon fiber bundle were completely dissolved. The CSY-F after water washing (denoted as WCSY-F) was folded into a U-shape with a size of 3 cm × 3 cm × 2 cm (length × width × height) and embedded in an expandable polyethylene (EPE) foam of approximately 10 mm thickness to enable the evaporator to float stably on the water surface. The produced CSY-F was placed in boiling water and left there overnight. The CSY-F was then repeatedly soaked with room temperature water until no foam was produced on the CSY-F surface. The vinylon yarns on the carbon fiber bundle were completely dissolved.

2.3. Characterization of the CSY and CSY-based fabric

The microscopic morphology of the various samples was examined using a field-emission scanning electron microscope (Sigma 500; Carl Zeiss AG, Germany) and a digital video microscope (RH-2000; HiROX, Japan). A ultraviolet–visible/near infrared (UV/vis/NIR) spectrometer (UV-3600Plus; Shimadzu, Japan) equipped with an integrated sphere was used to measure the optical transmittance and reflectance spectra of the sample surface. The absorption spectra of the samples were calculated according to $\alpha = 1 - \rho - \tau$, where α, ρ, and τ are the absorptivity, reflection, and transmission of the sample, respectively. The average solar absorptivity ($\bar{A}_{solar}$) in the full solar spectrum (0.3–2.5 μm) was calculated as: $\bar{A}_{solar} = \frac{\int_{0.3}^{2.5} I_{solar}(\lambda)A(\lambda)d\lambda}{\int_{0.3}^{2.5} I_{solar}(\lambda)d\lambda}$. Here $I_{solar}(\lambda)$ represents the solar intensity spectrum at air mass (AM) 1.5, and $A(\lambda)$ is the spectral absorptivity of a sample. A moisture management (MMT) test liquid moisture manager (m290; SDLATLAS, USA) was used to measure the ability of a sample to absorb water. Real-time heat distribution images were obtained using an infrared thermal imager (FLIR E8; Frestamp, USA). Temperature changes were constantly monitored using a multiplexed temperature recorder (TS-08A; SHSIWI, China). The ion concentration was measured using ICP-OES (Agilent 5110; Agilent Technologies Inc., USA).

2.4. Solar steam generation

Solar steam generation was conducted in a laboratory at constant temperature and humidity during the experiment. A solar simulator (CEL-HXF300-T3 photocatalytic xenon light source; China Education Au-light, China) was used to simulate sunlight. A power meter (CEL-NP2000-10 full-spectrum strong light power meter; China Education Au-light) was used to measure the radiation of the xenon lamp and maintain it at an illumination intensity of 1 $kW{\cdot}m^{-2}$ (1 sun). An electronic balance with an accuracy of 0.0001 g was used to record the mass change every ten seconds.

3. Results and discussion

3.1. Preparation of the CSY and CSY-based fabric

In addition to the carbon fiber and modal yarn, we selected vinylon yarns to improve the manufacturability of the carbon fibers. This is because the inherent rigidity of the carbon fiber can make weaving difficult. The preparation process of the CSYs and CSY-Fs is shown in Fig. 2(a), including spinning, CSY braiding, and fabric manufacturing. Vinylon yarn (14.6 tex, 20 °C water soluble; Fig. S1 in Appendix A) and carbon fiber filaments (60 tex) were first twisted together to form a VCCY in a fancy twister (Fig. 2(b)). More detailed spinning of the VCCY fabrication is shown in Movie S1 in Appendix A. The VCCYs were white in color (Fig. 2(c)) owing to the wrapping of the vinylon yarns. Fig. S2 in Appendix A shows that the carbon fiber was partially covered by vinylon yarns, which favored the protection of the carbon fiber during the entire weaving process. The CSYs were fabricated by wrapping the VCCYs over a super-hydrophilic modal yarn (Fig. 2(a)). An industrial 2D braiding machine (Fig. 2(d)) was used for the fabrication and mass production of the CSYs (Movie S2 in Appendix A). The CSYs produced by this method are shown in Fig. 2(e), which demonstrates that vinylon yarns can protect the carbon fiber during the entire braiding process. The CSYs were used as the warp, and carbon fiber (360 tex) was employed as the weft in CSY-F to produce a plain CSY-F in a weaving machine (Fig. 2(f)). Because of the solubility of the vinylon yarns in water, the CSY-F after water washing appeared black for solar interfacial evaporation (Fig. 2(g)). CSYs and CSY-Fs can

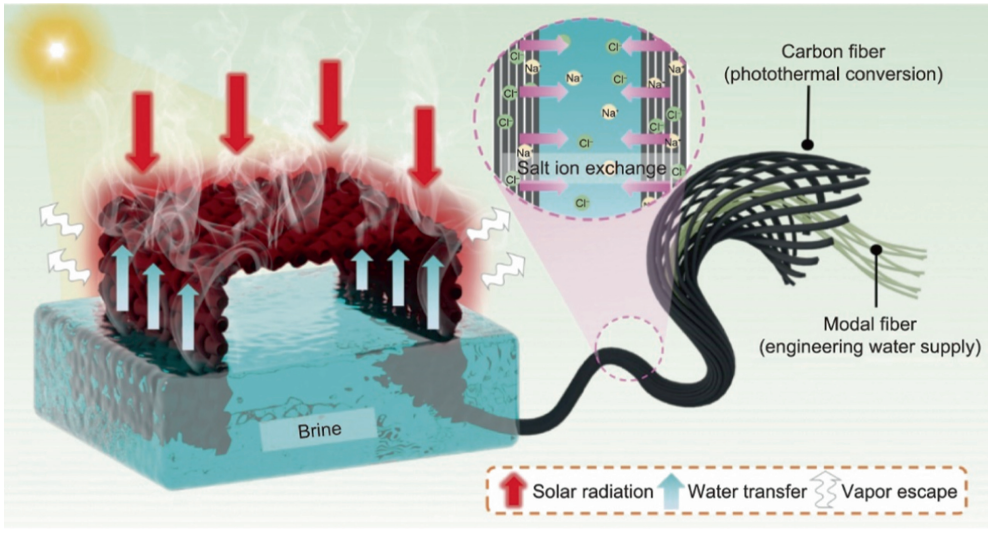

Fig. 1. Schematic illustration of a CSY-F and its solar desalination process under solar illumination.

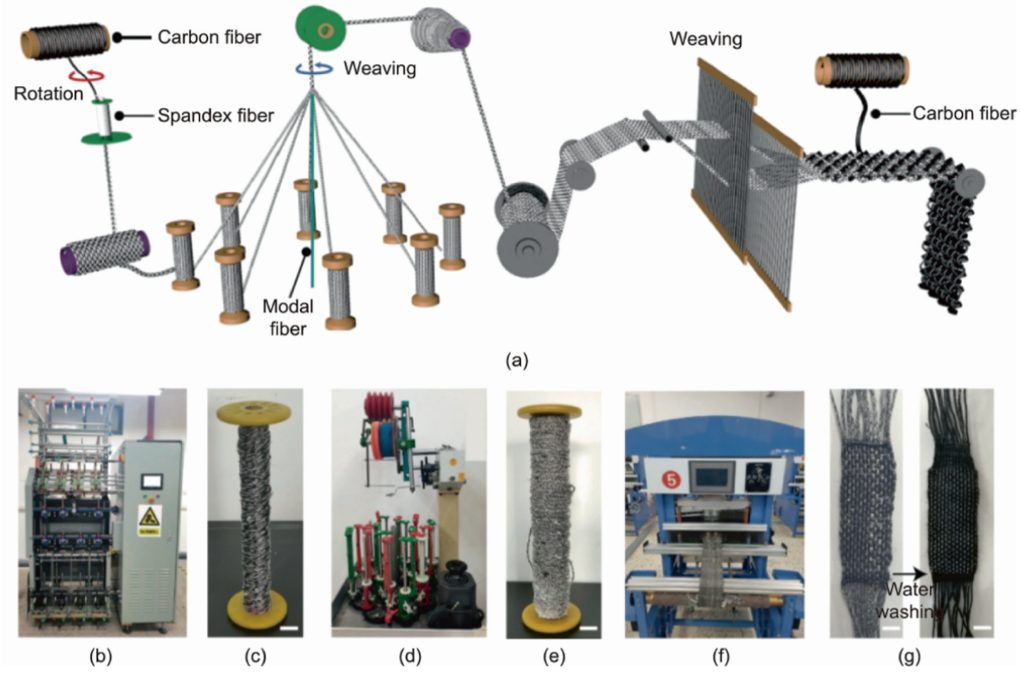

Fig. 2. Scalable and mass production for CSY and CSY-F. (a) Schematic illustration of the fabrication of core–sheath structure yarn and fabric. (b) Photograph of an industrial fancy twister. (c) Photograph of a package of VCCYs. Scale bar: 2 cm. (d) Photograph of a 2D braiding machine for fabricating core–sheath structure yarns. (e) Photograph of a package of CSYs. Scale bar: 2 cm. (f) Photograph of the weaving machine for fabricating CSY-F. (g) Photographs of a CSY-F before and after water washing. Scale bar: 1 cm.

adapt to the varying mechanical requirements of industrial weaving machines to meet the demand for scalable production.

3.2. Characterization

Fig. 3(a) shows a cross-section image of the CSY comprised of the core (the red arrow) and sheath layer of the WCSY. Fig. 3(b) shows the WCSY that appears after water washing. The WCSY appears to have a close and interactive weave, which can result in high light absorption via zigzag reflections. Laboratory tests measured the water pumping performance of the braided carbon fiber yarn without the core of the modal yarn (denoted as BCFY; Fig. S3 in Appendix A), and the WCSY with one strand of modal yarn (Figs. 3(c) and (d)). WCSY (Fig. 3(c)) and BCFY (Fig. 3(d)) (length: 50 mm) were simultaneously inserted vertically into a red dye solution. Although the wettability of the carbon fiber did not change (Fig. S4 in Appendix A), owing to the capillarity of the yarn, water could be pumped along the vertical direction of the yarn. As expected, we found that the core of the modal yarn can remarkably increase the liquid supply rate of the carbon fiber yarn. The white tissue paper at the top of the WCSY with one strand of modal yarn can be dyed red within 100 s (Fig. 3(c)). However, it takes 270 s for the dye to reach the top of the BCFY (Fig. 3(d)). Thus, balanced water transport of a CSY-F-based evaporator can be easily achieved by adjusting the number of modal yarns in the CSY during the weaving process. The three-dimensional (3D) micrographs of

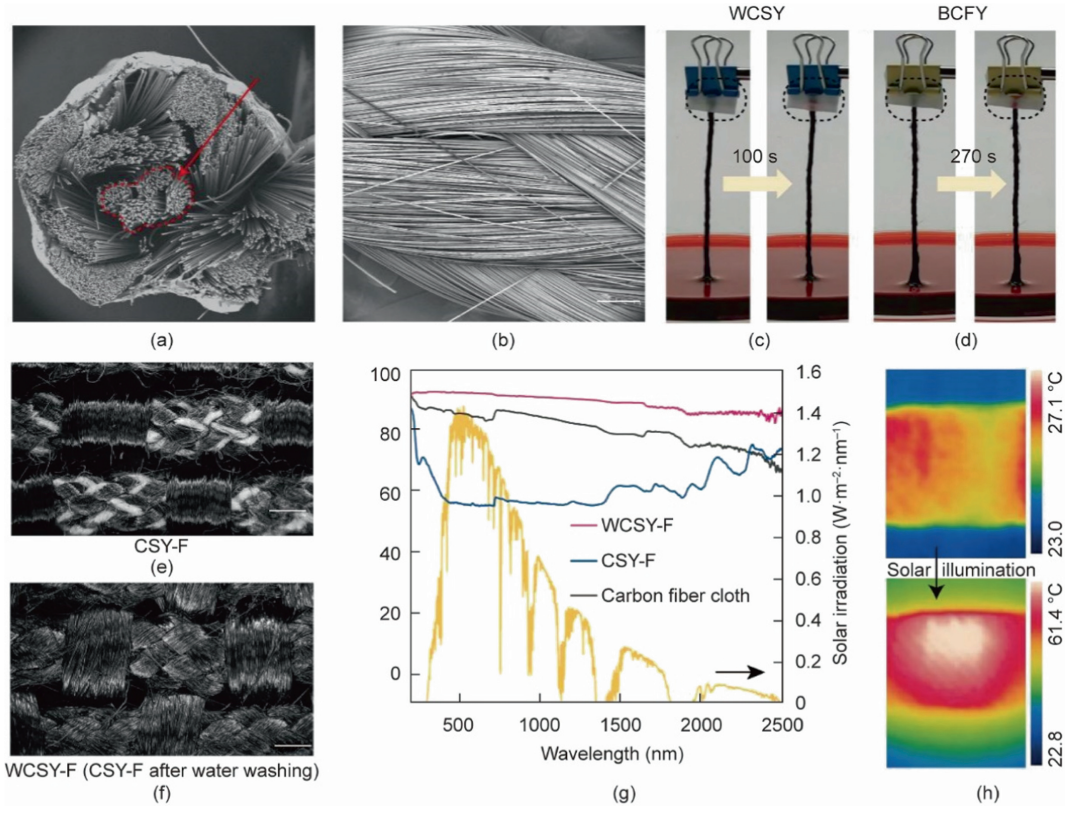

Fig. 3. Characterization of core–sheath structure yarn and fabric. (a) Scanning electron microscope (SEM) image of cores–heath structure yarn in the cross-section. The red arrow indicates the modal yarn core. Scale bar: 200 μm. (b) SEM image of core–sheath structure yarn in the surface section. Scale bar: 200 μm. The water pumping performance of (c) WCSY with one strand of modal yarn and (d) BCFY. 3D micrographs of (e) the CSY-F and (f) WCSY-F. Scale bar: 1 mm. (g) Absorptivity spectra of fabrics over the whole spectrum. The yellow curve: AM 1.5 Global solar spectrum. (h) The infrared images show the temperature of the WCSY-F one–sun illumination.

CSY-F and WCSY-F shown in Figs. 3(e) and (f) reveal that the vinylon yarn wrapped around the CSY can be washed off completely in water. An absorptive test was performed to evaluate the photothermal performance of CSY-F. The light absorption properties over the entire solar spectrum (Fig. 3(g)) indicate that CSY-F had a significant photothermal effect. Absorptivity testing revealed that the absorptivity over the entire solar spectrum of WCSY-F (92%) was significantly higher than that of the carbon fiber cloth (58%) and CSY-F (85%). Under one-sun illumination, the surface temperature of WCSY-F can reach up to 61.4 °C (Fig. 3(h)), indicating high photothermal conversion performance.

3.3. Photothermal evaporation performance

Engineering a controllable water supply is a critical factor in boosting interfacial evaporation performance [23,37,38]. The core modal yarn in our CSY design can adjust its water-pumping performance (see Fig. 3(c)). We adjusted the number of core modal yarns in the CSY to investigate the photothermal evaporation performance of different water supplies. In Fig. 4(a), three CSYs with 0, 8, and 16 strands of modal yarn were designed for the WCSY-F-based evaporators. After water washing, these CSYs are denoted as 0-WCSY-F, 8-WCSY-F, and 16-WCSY-F, respectively. The corresponding WCSY-based evaporators are denoted as 0-WCSY-F, 8-WCSY-F, and 16-WCSY-F, respectively. Fig. 4(b) shows 3D cross-section micrographs of 0-WCSY, 8-WCSY, and 16-WCSY.

Compared with 0-WCSY (Fig. S5(a) in Appendix A), 8-WCSY exhibits faster water pumping owing to the core modal yarns in the CSY (Fig. S5(b)); its water pumping performance is comparable to that of 16-WCSY (Fig. S5(c)). We used an MMT (Fig. S6(a) in Appendix A) to investigate the engineering-controllable water supply of the core modal yarn. The relative water content of the corresponding WCSY-Fs was proportional to the number of core modal yarns in the CSY (Fig. S6(b)). Fig. S7 in Appendix A shows that the wettability of the WCSY-Fs was remarkably different after 1 h of illumination. This demonstrates the ability of the core modal yarn to be engineered for a controllable water supply. Further, the number of core modal yarns in the CSY did not affect the optical properties (Fig. S8 in Appendix A), mechanical strength (Fig. S9 in Appendix A), or thermal conductivity (Fig. S10 in Appendix A) of the WCSY-Fs. To evaluate the photothermal performance of the CSY-F-based evaporators, evaporation experiments were conducted in a laboratory environment (temperature, (22 ± 1) °C; humidity, 50% ± 5%). The container was surrounded by thermal insulation (foam) and aluminum foil to eliminate solar energy and heat the bulk water (Fig. 4(c)). As shown in Fig. 4(d), the core modal yarn of the CSYs was designed to adjust the supply of water, while the sheath carbon fiber converted solar energy into heat. The synergistic effect of the two components in the CSYs resulted in excellent interfacial evaporation performance. First, we tested the temperature changes of 0-WCSY-F, 8-WCSY-F, and 16-WCSY-F under one-sun illumination. The temperature distribution in the infrared (IR) images of the CSY-Fs (inset in Fig. 4(e)) demonstrated that the three WCSY-Fs could efficiently utilize solar energy to produce steam. However, owing to the different water supplies, the real-time temperature of WCSY-Fs using a temperature detector showed differences (Fig. 4(e)). The heating rates of 0-WCSY-F and 8-WCSY-F were relatively close to but higher than those of 16-WCSY-F. The difference in the temperature variations of the three WCSY-Fs indicated that they had different photothermal

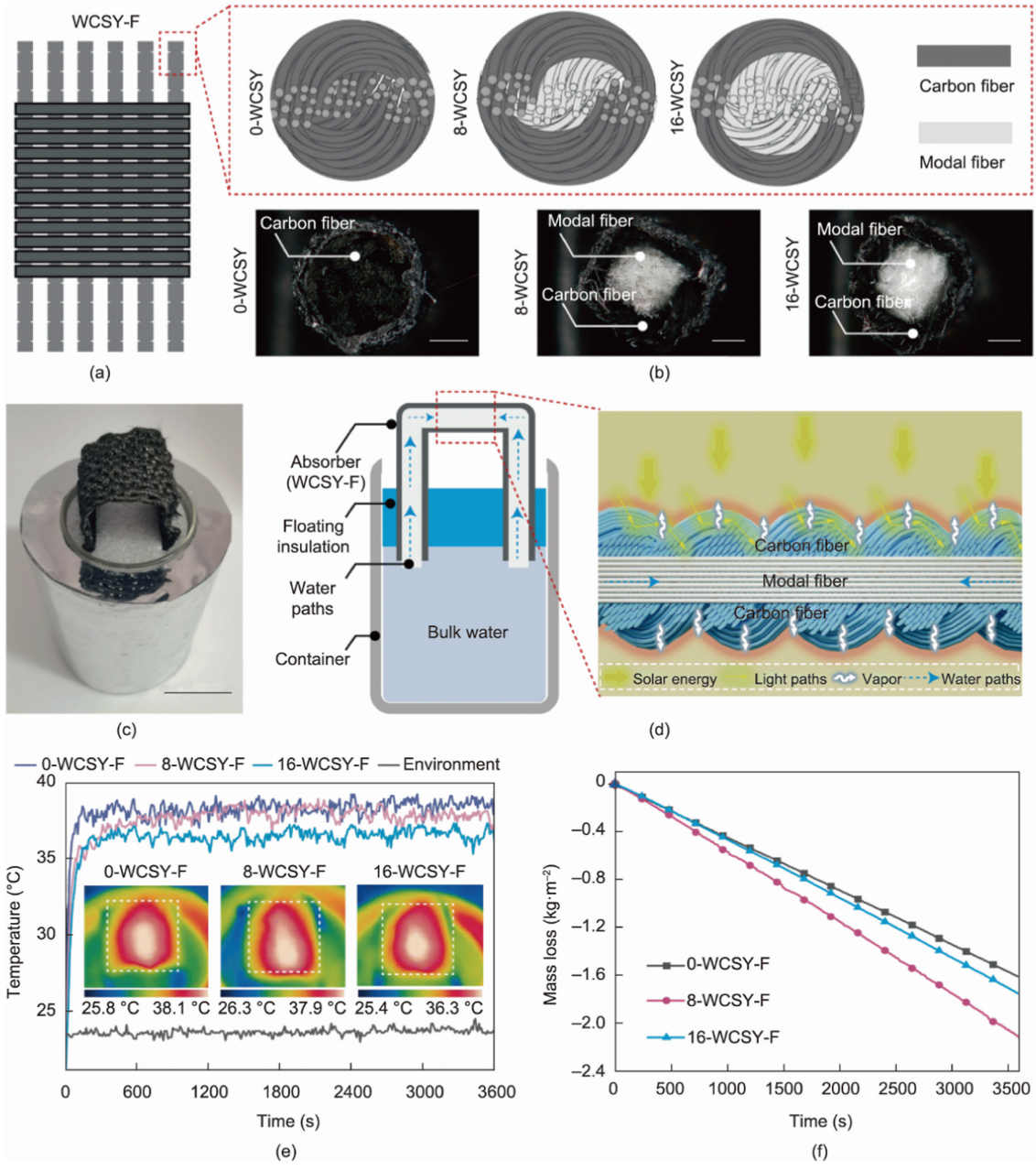

Fig. 4. Photothermal evaporation of the fabric-based evaporator. (a) Schematic illustration of the fabric-based evaporator with different water supply. Three CSYs with 0, 8, and 16 beams modal yarn were applied in WCSY-F-based evaporators, which are named 0-WCSY-F, 8-WCSY-F, and 16-WCSY-F, respectively. (b) 3D micrographs of 0-WCSY, 8-WCSY, and 16-WCSY at the cross-section. Scale bar: 500 μm. (c) Photograph of the evaporation still. Scale bar: 2 cm. (d) Schematic diagram of the CSY-F-based evaporator realizing fast solar-thermal water evaporation. (e) Temperature response of the 0-WCSY-F, 8-WCSY-F, and 16-WCSY-F over one hour under one–sun illumination and the IR imaging photographs of these WCSY-Fs after one-hour illumination. (f) Mass losses of the 0-WCSY-F, 8-WCSY-F, and 16-WCSY-F, when treating DI water under one–sun illumination.

conversion efficiencies. The deionized (DI) water evaporation rate of the WCSY-F-based evaporators was tested under one-sun illumination. The evaporation curves of the evaporators are shown in Fig. 4(f). As the quantity of core modal yarn increases in CSYs, the evaporation rate first exhibits an increasing and then a decreasing trend. As shown in Figs. S11 and S12 in Appendix A, the evaporation rates and photothermal conversion efficiency of 0-WCSY-F, 8-WCSY-F, and 16-WCSY-F were also calculated to be 1.60 $kg \cdot m^{-2} \cdot h^{-1}$ (63.4%), 2.12 $kg \cdot m^{-2} \cdot h^{-1}$ (93.7%), and 1.75 $kg \cdot m^{-2} \cdot h^{-1}$ (75.3%), respectively. The evaporation results show that the optimized number of core modal yarns in the CSYs is eight, revealing that 8-WCSY-F can achieve a balanced water supply. The value is comparable to that of high-performance solar evaporators with controllable water supply reported previously under one-sun illumination (Fig. S13 in Appendix A).

3.4. Durable salt-rejection

Because salt accumulation at absorbers is a critical factor in lowering the performance of evaporators during solar interfacial evaporation [39–41], we conducted a long-term simulated seawater (5 wt% NaCl solution) evaporation experiment for 8 h in the laboratory. As shown in Fig. 5(a), the salt gradually accumulated on the surface of the 8-WCSY-F-based evaporator, in which two water paths wicked water to its top for solar evaporation. The WCSY-F-based evaporator with different water paths is denoted as the

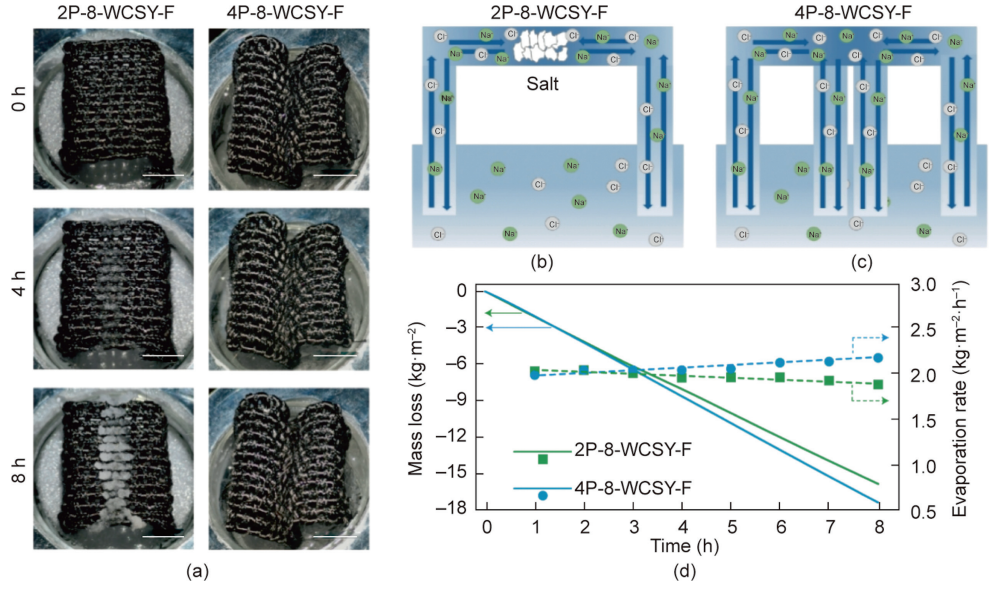

Fig. 5. The durable salt-rejection of the fabric-based evaporator. (a) Photographs of the 2P-8-WCSY-F and 4P-8-WCSY-F over time when treating 5 wt% NaCl solution (the WCSY-F-based evaporator with different water paths is denoted as the *X*P-8-WCSY-F-based evaporator, where *X* is the number of water paths). Scale bar: 1 cm. Schematic of the salt crystallization in the (b) 2P-8-WCSY-F and (c) 4P-8-WCSY-F. (d) Mass losses and evaporation rates of the 2P-8-WCSY-F and 4P-8-WCSY-F over 8 hours.

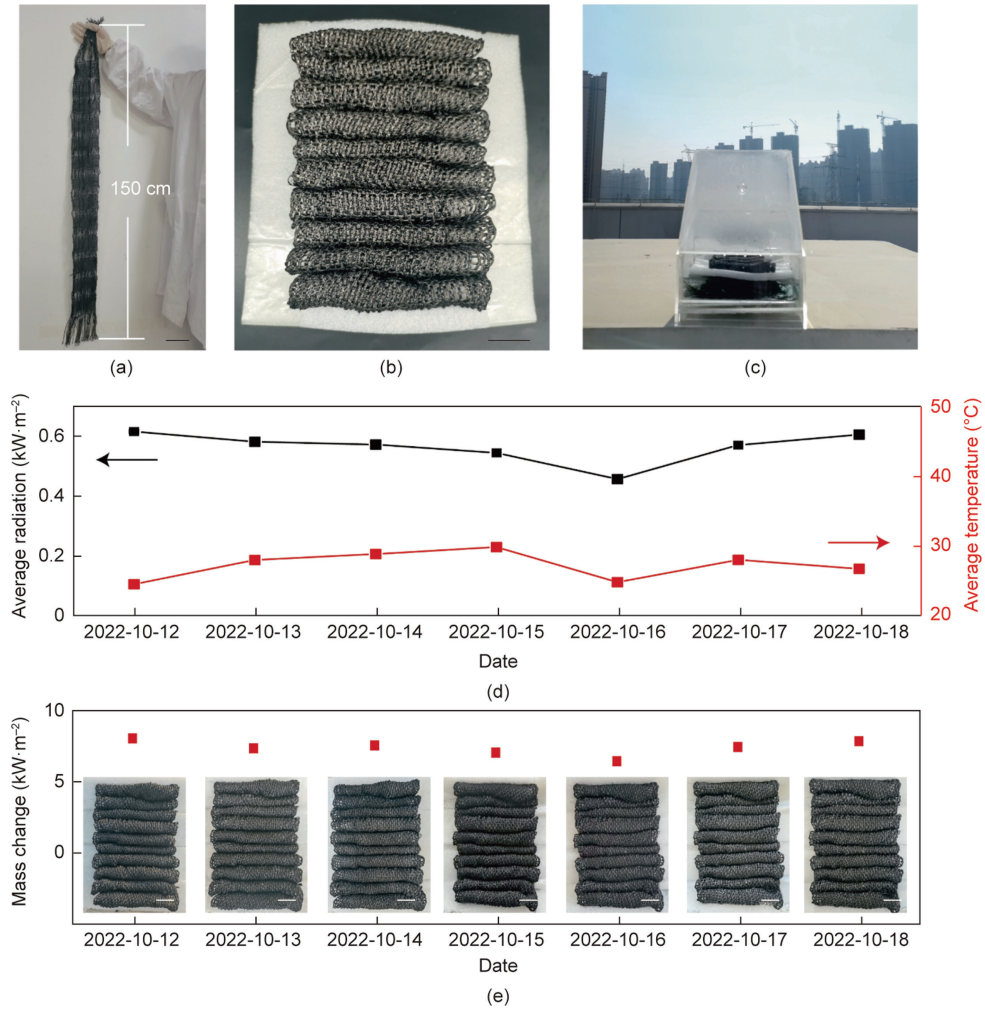

Fig. 6. Outdoor test of the WCSY-F-based evaporator. Photographs of (a) the large-scale WCSY-F for an outdoor test (scale bar: 10 cm) and (b) the corresponding WCSY-F-based evaporator (scale bar: 2 cm). (c) Photograph of the still in operation at the roof of Wuhan Textile University. (d) The average solar irradiation intensity and temperature from October 12 to 18, 2022, at Wuhan, China. (e) The mass changes of water during the continuous outdoor test. Inserts are photograph of the CSY-F-based evaporator after desalination. Scale bar: 2 cm.

*X*P-8-WCSY-F-based evaporator, where *X* is the number of water paths. However, owing to fast natural convection in the two water supply paths [16,42,43] (Fig. 5(b)), an appreciable amount of salt can only be found in the middle of 8-WCSY-F. Next, owing to the unique flexibility of fabrics, we added two extra water paths for salt diffusion via an origami design (4P-8-WCSY-F). As expected, the surface of 4P-8-WCSY-F showed no obvious change during 8 h of evaporation in the 5 wt% NaCl solution (Fig. 5(a)) owing to the addition of the extra two water paths (Fig. 5(c)). As shown in Fig. 5(d), the evaporation rates of 4P-8-WCSY-F and 2P-8-WCSY-F were relatively close during the first two hours of evaporation, which indicates that the addition of salt diffusion paths in the 8-WCSY-F-based evaporator did not influence its evaporation performance. However, owing to salt accumulation at 2P-8-WCSY-F after four hours of solar illumination, the evaporation rate of 2P-8-WCSY-F shows a downward trend. During continuous one-sun illumination for 8 h, the evaporation rates of 4P-8-WCSY-F were maintained at a high level. Furthermore, 4P-0-WCSY-F and 4P-16-WCSY-F were used to test their stability after eight hours of one-sun illumination in a 5 wt% NaCl solution. The mass change of the liquid with the WCSY-F-based evaporators evolved almost linearly (Fig. S14(a) in Appendix A). As shown in Fig. S14(b), the evaporation rates of 4P-8-WCSY-F and 4P-16-WCSY-F were maintained at high levels. Similar to DI water, the evaporation rates of 4P-8-WCSY-F were higher than those of 4P-0-WCSY-F and 4P-16-WCSY-F during the long-term solar desalination. The decrease in evaporation rates of 4P-0-WCSY-F can be attributed to salt accumulation at its surface during the long-duration test (Fig. S13(c)). An outdoor experiment was performed to collect the vapor generated by light irradiation to evaluate the desalination performance of the evaporator (Fig. S15(a) in Appendix A). As shown in Fig. S15(b), the ion concentration in the condensed water (Na^+: 0.64 mg·L^{-1}, B^{3+}: 0.13 mg·L^{-1}, K^+: 0.086 mg·L^{-1}, Mg^{2+}: 0.17 mg·L^{-1}, Ca^{2+}: 0.76 mg·L^{-1}) met the healthy drinking water standards set by the World Health Organization.

3.5. Large-scale outdoor test

To further verify the performance of the WCSY-F-based evaporator under realistic weather conditions, we conducted a continuous outdoor experiment on sunny days. Because both CSYs and CSY-Fs were fabricated by industrial weaving methods, a larger-scale WCSY-F (Fig. 6(a)) was easy to fabricate in our laboratory. The large-scale WCSY-F-based evaporator is shown in Fig. 6(b).

According to the results described in Section 3.3, the optimized number of modal yarns in CSY is eight strands for this larger-scale WCSY-F-based evaporator. Fig. 6(c) shows the outdoor testing equipment where highly transparent plexiglass is used to enable sunlight absorption of the larger-scale WCSY-F. A pyranometer (Fig. S16 in Appendix A) was used to record the incident solar flux and environmental temperature. The experiment began at 09:00 (local time) and ended at 17:00 (local time). Fig. S17 in Appendix A and Fig. 6(d) show the weather conditions during seven days of experiments (October 12 to 18, 2022). As displayed in Fig. 6(e), the steam yield was at a rate of about 7.5 L·m^{-2}·d^{-1} and no obvious salt could be found during the continuous outdoor experiment, which proves that this fabric-based evaporator with an engineering water supply has excellent stability on-site.

4. Conclusions

We reported a versatile core–sheath photothermal yarn and demonstrated a fabric-based evaporator via a large-scale weaving technique for stable and efficient solar interfacial desalination. With modal yarn (core layer) and carbon fiber (sheath layer) as the water channels and photothermal material, respectively, a versatile yarn was obtained using a large-scale 2D braiding technique. The employed innovative yarn structure demonstrated its photothermal performance under the sun and provided a sufficient water supply for water evaporation. Experimentation showed that balanced water could easily be achieved (because of the poor water pumping of the carbon fiber) by adjusting the number of core modal yarns. This enabled stable and efficient solar interfacial desalination. In addition, both core–sheath structure photothermal yarns and fabric-based evaporators were fabricated via traditional textile technology, which demonstrates the practical feasibility of large-scale applications.

Authors' contribution

Xingfang Xiao: methodology, investigation, data curation, writing — original draft. **Luqi Pan:** methodology, investigation, data curation, writing — original draft. **Tao Chen:** methodology, validation, investigation. **Manyu Wang:** methodology, validation, investigation. **Lipei Ren:** methodology, validation. **Bei Chen:** methodology, validation. **Yingao Wang:** validation, investigation. **Qian Zhang:** conceptualization, supervision. **Weilin Xu:** conceptualization, supervision.

Acknowledgment

We acknowledge the financial support from the National Natural Science Foundation of China (52103064 and U21A2095), the Key Research and Development Program of Hubei Province (2021BAA068), and National Local Joint Laboratory for Advanced Textile Processing and Clean Production (FX2022001).

Appendix A. Supplementary data

Supplementary data to this article can be found online at https://doi.org/10.1016/j.eng.2023.03.015.

References

[1] Bian Y, Tian Y, Tang K, Li W, Zhao L, Yang Y, et al. Sustainable solar evaporation from solute surface via energy downconversion. Glob Chall 2021;5(1):2000077.
[2] Jamieson AJ, Brooks LSR, Reid WDK, Piertney SB, Narayanaswamy BE, Linley TD. Microplastics and synthetic particles ingested by deep-sea amphipods in six of the deepest marine ecosystems on Earth. R Soc Open Sci 2019;6(2):180667.
[3] Falconer RA. Water security: why we need global solutions. Engineering 2022;16:13–5.
[4] Zhou W, Zhang X, Gong X, Ding M, Yu J, Zhang S, et al. Environmentally friendly polyamide nanofiber membranes with interconnective amphiphobic channels for seawater desalination. ACS Appl Mater Interfaces 2022;14(30):35287–96.
[5] Yoon J, Kwon HJ, Kang S, Brack E, Han J. Portable seawater desalination system for generating drinkable water in remote locations. Environ Sci Technol 2022;56(10):6733–43.
[6] Yao W, Zhu X, Xu Z, Davis RA, Liu G, Zhong H, et al. Loofah sponge-derived hygroscopic photothermal absorber for all-weather atmospheric water harvesting. ACS Appl Mater Interfaces 2022;14(3):4680–9.
[7] Elimelech M, Phillip WA. The future of seawater desalination: energy, technology, and the environment. Science 2011;333(6043):712–7.
[8] Liu H, Huang Z, Liu K, Hu X, Zhou J. Interfacial solar-to-heat conversion for desalination. Adv Energy Mater 2019;9(21):1900310.
[9] Zhang P, Liao Q, Yao H, Huang Y, Cheng H, Qu L. Direct solar steam generation system for clean water production. Energy Stor Mater 2019;18:429–46.
[10] Yang Y, Zhao R, Zhang T, Zhao K, Xiao P, Ma Y, et al. Graphene-based standalone solar energy converter for water desalination and purification. ACS Nano 2018;12(1):829–35.
[11] Gao M, Zhu L, Peh CK, Ho GW. Solar absorber material and system designs for photothermal water vaporization towards clean water and energy production. Energ Environ Sci 2019;12(3):841–64.
[12] Xie Z, Duo Y, Lin Z, Fan T, Xing C, Yu L, et al. The rise of 2d photothermal materials beyond graphene for clean water production. Adv Sci 2020;7(5):1902236.
[13] Zhou X, Guo Y, Zhao F, Yu G. Hydrogels as an emerging material platform for solar water purification. Acc Chem Res 2019;52(11):3244–53.

[14] Zhu L, Gao M, Peh CKN, Ho GW. Solar-driven photothermal nanostructured materials designs and prerequisites for evaporation and catalysis applications. Mater Horiz 2018;5(3):323–43.
[15] Zhu L, Gao M, Peh CKN, Ho GW. Recent progress in solar-driven interfacial water evaporation: advanced designs and applications. Nano Energy 2019;57:507–18.
[16] Zhang Y, Xiong T, Nandakumar DK, Tan SC. Structure architecting for salt-rejecting solar interfacial desalination to achieve high-performance evaporation with *in situ* energy generation. Adv Sci (Weinheim, Ger) 2020; 7(9):1903478.
[17] Hu X, Zhu J. Tailoring aerogels and related 3D macroporous monoliths for interfacial solar vapor generation. Adv Funct Mater 2020; 30(3):1907234.
[18] Zhang L, Li X, Zhong Y, Leroy A, Xu Z, Zhao L, et al. Highly efficient and salt rejecting solar evaporation via a wick-free confined water layer. Nat Commun 2022;13(1):849.
[19] Li T, Liu H, Zhao X, Chen G, Dai J, Pastel G, et al. Scalable and highly efficient mesoporous wood-based solar steam generation device: localized heat, rapid water transport. Adv Funct Mater 2018;28(16):1707134.
[20] Lu Y, Fan D, Wang Y, Xu H, Lu C, Yang X. Surface patterning of two-dimensional nanostructure-embedded photothermal hydrogels for high-yield solar steam generation. ACS Nano 2021;15(6):10366–76.
[21] Liang H, Liao Q, Chen N, Liang Y, Lv G, Zhang P, et al. Thermal efficiency of solar steam generation approaching 100% through capillary water transport. Angew Chem Int Ed Engl 2019;58(52):19041–6.
[22] Li J, Wang X, Lin Z, Xu N, Li X, Liang J, et al. Over 10 kg m^{-2} h^{-1} evaporation rate enabled by a 3D interconnected porous carbon foam. Joule 2020; 4(4):928–37.
[23] Tao P, Ni G, Song C, Shang W, Wu J, Zhu J, et al. Solar-driven interfacial evaporation. Nat Energy 2018;3(12):1031–41.
[24] Li Z, Wang C, Su J, Ling S, Wang W, An M. Fast-growing field of interfacial solar steam generation: evolutional materials, engineered architectures, and synergistic applications. Sol RRL 2019;3(3):1800206.
[25] Li Y, Jin X, Zheng Y, Li W, Zheng F, Wang W, et al. Tunable water delivery in carbon-coated fabrics for high-efficiency solar vapor generation. ACS Appl Mater Interfaces 2019;11(50):46938–46.
[26] Li Z, Zhang J, Zang S, Yang C, Liu Y, Jing F, et al. Engineering controllable water transport of biosafety cuttlefish juice solar absorber toward remarkably enhanced solar-driven gas–liquid interfacial evaporation. Nano Energy 2020;73:104834.
[27] Wang Z, Wu X, He F, Peng S, Li Y. Confinement capillarity of thin coating for boosting solar-driven water evaporation. Adv Funct Mater 2021;31 (22):2011114.
[28] Zhu R, Liu M, Hou Y, Wang D, Zhang L, Wang D, et al. Mussel-inspired photothermal synergetic system for clean water production using full-spectrum solar energy. Chem Eng J 2021;423:129099.
[29] Tang J, Zheng T, Song Z, Shao Y, Li N, Jia K, et al. Realization of low latent heat of a solar evaporator via regulating the water state in wood channels. ACS Appl Mater Interfaces 2020;12(16):18504–11.
[30] Zhang C, Xiao P, Ni F, Gu J, Chen J, Nie Y, et al. Breathable and superhydrophobic photothermic fabric enables efficient interface energy management via confined heating strategy for sustainable seawater evaporation. Chem Eng J 2022;428:131142.
[31] Li T, Fang Q, Xi X, Chen Y, Liu F. Ultra-robust carbon fibers for multi-media purification via solar-evaporation. J Mater Chem A Mater Energy Sustain 2019;7(2):586–93.
[32] Fang Q, Li T, Lin H, Jiang R, Liu F. Highly efficient solar steam generation from activated carbon fiber cloth with matching water supply and durable fouling resistance. ACS Appl Energy Mater 2019;2(6):4354–61.
[33] Li H, He Y, Hu Y, Wang X. Commercially available activated carbon fiber felt enables efficient solar steam generation. ACS Appl Mater Interfaces 2018;10 (11):9362–8.
[34] Yu Z, Cheng S, Li C, Li L, Yang J. Highly efficient solar vapor generator enabled by a 3D hierarchical structure constructed with hydrophilic carbon felt for desalination and wastewater treatment. ACS Appl Mater Interfaces 2019;11 (35):32038–45.
[35] Zhou HW, Mishnaevsky Jr L, Yi HY, Liu YQ, Hu X, Warrier A, et al. Carbon fiber/carbon nanotube reinforced hierarchical composites: effect of CNT distribution on shearing strength. Compos B Eng 2016;88:201–11.
[36] Ma A, Chen Y, Liu Y, Gui J, Yu Y. Reduced graphene oxide/carbon fiber composite membrane for self-floating solar-thermal steam production. Chem Res Chin Univ 2020;36(4):699–702.
[37] Pang Y, Zhang J, Ma R, Qu Z, Lee E, Luo T. Solar-thermal water evaporation: a review. ACS Energy Lett 2020;5(2):437–56.
[38] Xu Z, Li Z, Jiang Y, Xu G, Zhu M, Law WC, et al. Recent advances in solar-driven evaporation systems. J Mater Chem A Mater Energy Sustain 2020;8 (48):25571–600.
[39] Xu N, Li J, Wang Y, Fang C, Li X, Wang Y, et al. A water lily-inspired hierarchical design for stable and efficient solar evaporation of high-salinity brine. Sci Adv 2019;5(7):eaaw7013.
[40] Xu N, Zhang H, Lin Z, Li J, Liu G, Li X, et al. A scalable fish-school inspired self-assembled particle system for solar-powered water-solute separation. Natl Sci Rev 2021;8(10):nwab065.
[41] Zhou L, Li X, Ni GW, Zhu S, Zhu J. The revival of thermal utilization from the Sun: interfacial solar vapor generation. Natl Sci Rev 2019;6(3):562–78.
[42] Ni G, Zandavi SH, Javid SM, Boriskina SV, Cooper TA, Chen G. A salt-rejecting floating solar still for low-cost desalination. Energy Environ Sci 2018;11 (6):1510–9.
[43] Zhang Q, Xiao X, Zhao G, Yang H, Cheng H, Qu L, et al. An all-in-one and scalable carbon fibre-based evaporator by using the weaving craft for high-efficiency and stable solar desalination. J Mater Chem A Mater Energy Sustain 2021;9(17):10945–52.